



## Article

# Insights into Very Early Afterslip Associated with the 2021 M 8.2 Chignik, Alaska Earthquake Using Subdaily GNSS Solutions

Yunfei Xiang <sup>1,2</sup> , Yankai Bian <sup>3,\*</sup>, Jie Liu <sup>1</sup> and Yin Xing <sup>4</sup>

<sup>1</sup> College of Civil Engineering, Nanjing Forestry University, Nanjing 210037, China; yfxiang@njfu.edu.cn (Y.X.); jieliu@njfu.edu.cn (J.L.)

<sup>2</sup> College of Oceanography, Hohai University, Nanjing 210024, China

<sup>3</sup> School of Geomatics and Municipal Engineering, Zhejiang University of Water Resources and Electric Power, Hangzhou 310018, China

<sup>4</sup> School of Geography Science and Geomatics Engineering, Suzhou University of Science and Technology, Suzhou 215009, China; xingyin@usts.edu.cn

\* Correspondence: bianyk@zjweu.edu.cn; Tel.: +86-188-5200-0536

**Abstract:** Based on subdaily kinematic GNSS solutions, the fault slip properties during the very early postseismic phase after the 2021 M 8.2 Chignik earthquake are investigated in this paper. The very early postseismic deformations captured by near-field GNSS sites can be well depicted by the power model. The comparison of afterslip determined by daily and subdaily GNSS solutions suggests that neglecting very early afterslip can result in the underestimation of postseismic slip. Compared with coseismic slip, the cumulative afterslip of the first 24 h is mainly focused in the southeast of the hypocenter, and the shallow updip afterslip appears after this earthquake. The spatio-temporal evolution of the afterslip reveals that the patch of afterslip is immediately generated after the earthquake, and then the postseismic slip gradually grows along the afterslip patch. The magnitude of the afterslip patch varies remarkably within the 24 h following the earthquake, especially in the first several hours. Meanwhile, the spatio-temporal patterns of aftershocks and afterslip exhibit strong similarity during the first 24 h, suggesting that very early afterslip may be a possible driving factor of aftershocks. Moreover, most of the afterslip patches and aftershocks occurring immediately after this earthquake are situated in the area covered by positive Coulomb Stress Change (CSC), which implies that the immediate afterslip and aftershock activities can be influenced by the coseismic CSC. The following afterslip process further releases coseismic CSC and then influences the spatio-temporal variations of aftershock activities. Thus, the afterslip may be a possible triggering mechanism of very early aftershocks for this earthquake, alongside the effects of the CSC generated by coseismic rupture.

**Keywords:** GNSS; very early afterslip; spatio-temporal pattern; aftershock; triggering mechanism



**Citation:** Xiang, Y.; Bian, Y.; Liu, J.; Xing, Y. Insights into Very Early Afterslip Associated with the 2021 M 8.2 Chignik, Alaska Earthquake Using Subdaily GNSS Solutions. *Remote Sens.* **2023**, *15*, 5469. <https://doi.org/10.3390/rs15235469>

Academic Editors: Pablo Rodríguez-González and Diego González-Aguilera

Received: 17 September 2023  
Revised: 18 November 2023  
Accepted: 21 November 2023  
Published: 23 November 2023



**Copyright:** © 2023 by the authors. Licensee MDPI, Basel, Switzerland. This article is an open access article distributed under the terms and conditions of the Creative Commons Attribution (CC BY) license (<https://creativecommons.org/licenses/by/4.0/>).

## 1. Introduction

In general, significant postseismic deformations can be observed after many large tectonic earthquakes [1–4]. The fault healing mechanisms and the rheological properties of the Earth's lithosphere can be explored by investigating the postseismic process [5–9]. Currently, characterizing the postseismic deformation mechanism mainly relies on daily Global Navigation Satellite System (GNSS) position time series and Interferometric Synthetic Aperture Radar (InSAR) observations [10]. The temporal resolution of the two geodetic observations does not allow us to understand the transient postseismic deformations within the time scales of minutes to hours after the earthquake. On the other hand, the subdaily postseismic process is of great importance to accurately determine the amount of postseismic slip and understand the transition process between coseismic rupture and postseismic relaxation [11,12]. Meanwhile, the afterslip–aftershock relationship that exists in the postseismic phase has gradually attracted the attention of some scholars [13–17]. However, previous studies associated with afterslip–aftershock relationship mainly focus

on the time scales of days to months due to the limitation of the temporal resolution of observations. Thus, the afterslip–aftershock relationship within the initial postseismic phase can be further explored using higher temporal resolution observations, which helps to understand the triggering mechanisms of early aftershocks.

Recently, some studies have investigated the fault activities during the very early postseismic phase based on subdaily GNSS solutions. Tsang et al. [18] imaged the early afterslip distribution of the 2016 Pedernales earthquake using kinematic and static GNSS solutions, which highlighted that the postseismic slip could be greatly underestimated if the very early postseismic deformations were neglected. Milliner et al. [19] determined the moment release and frictional properties of very early afterslip after the 2016 Kumamoto earthquake and found that the seismogenic fault entered the deceleration phase directly after coseismic rupture without nucleation or acceleration process. Jiang et al. [20] revealed the multiphase scenario of afterslips and aftershocks following the 2004 Parkfield earthquake, which confirmed that the early afterslips and associated stress variations that occurred synchronized with aftershock activities. The results also suggested that afterslip plays an important role in the seismicity modulation after the earthquake. Liu et al. [21] adopted a 1 Hz GNSS position time series to image the evolution of the very early afterslip, and compared the result with the afterslip estimated by daily GNSS solutions. The afterslip and aftershocks displayed similar spatio-temporal distribution, suggesting that aftershock activities could be affected by afterslip behaviors. Perillat et al. [22] investigated the early postseismic process using the kinematic 15 s GNSS solutions after the 2011 Tohoku-Oki earthquake, and proposed that early afterslip could be explained by the transient brittle creep mechanism. These studies jointly highlight the rich geophysical information contained in very early postseismic processes, which can contribute to a better understanding of fault behaviors and aftershock triggering mechanisms.

On 29 July 2021, an M 8.2 earthquake with a focal depth of 35 km occurred 99 km (55.364°N, 157.888°W) southeast of Perryville, Alaska. The earthquake was induced by a shallow thrust fault at the interface of the subduction zone between the Pacific and North American plates, where the Pacific plate began subducting to the northwest beneath Alaska. Many strong earthquakes have struck the Alaska–Aleutian subduction zone as a consequence of the subduction of the Pacific plate [23–26]. Thus far, some studies have revealed the crustal deformations, fault slip properties, and stress changes associated with this earthquake based on geodetic and seismological observations. Liu et al. [27] resolved a fine coseismic slip of the 2021 Chignik earthquake by the combined use of teleseismic broadband waveforms and high-rate GNSS observations. Elliott et al. [28] also displayed a coseismic slip and discussed the relationship between this earthquake and other large earthquakes in the Alaska subduction zone. Brooks et al. [29] determined the rapid afterslip after the 2021 Chignik earthquake, and seafloor geodetic observations were utilized for the first time. On the other hand, few studies focus on the very early postseismic deformations within the first minutes to hours after this earthquake, as well as the fault mechanism evolution in this time scale.

Based on the above discussion, we first detect the very early postseismic deformations after this earthquake using subdaily GNSS solutions. Then, the spatio-temporal properties of very early afterslip are characterized by modeled postseismic signals. Meanwhile, we also assess the afterslip–aftershock relationship by comparing the spatial–temporal distribution of afterslips and aftershocks. Finally, we evaluate the contributions of the very early afterslip to the postseismic slip according to the comparison of the afterslip estimated by daily and subdaily GNSS solutions. Generally, the stress state around the coseismic rupture area can be altered after the earthquake, which is considered to be related to postseismic activities. Moreover, the coseismic Coulomb stress changes associated with this earthquake are determined, which are utilized to further explore the triggering mechanism of aftershocks.

## 2. Datasets and Methods

### 2.1. GNSS Observations

In order to detect the very early postseismic deformations following this earthquake, the 15 s GNSS observations of 9 near-field sites derived from the NSF's Network of the Americas (NOTA) operated by the University NAVSTAR Consortium (UNAVCO) are collected (Figure 1). The 15 s GNSS observations with the time span of 3 days before and 7 days after this earthquake are processed by the PPP-AR software developed by the PRIDE research group of Wuhan University [30–32]. Based on the PPP-AR software, Precision Point Positioning (PPP) with Ambiguity Resolution (AR) is conducted for raw GNSS observations to obtain kinematic solutions. The tropospheric delay is corrected by Vienna Mapping Functions 1 (VMF1), and the high-order ionospheric error is corrected using GIM products [33–35]. Meanwhile, the effects of solid tide, ocean tide, and polar tide are also corrected. The code bias, phase bias, precision satellite orbit, and clock products provided by Wuhan University are adopted during the data processing.

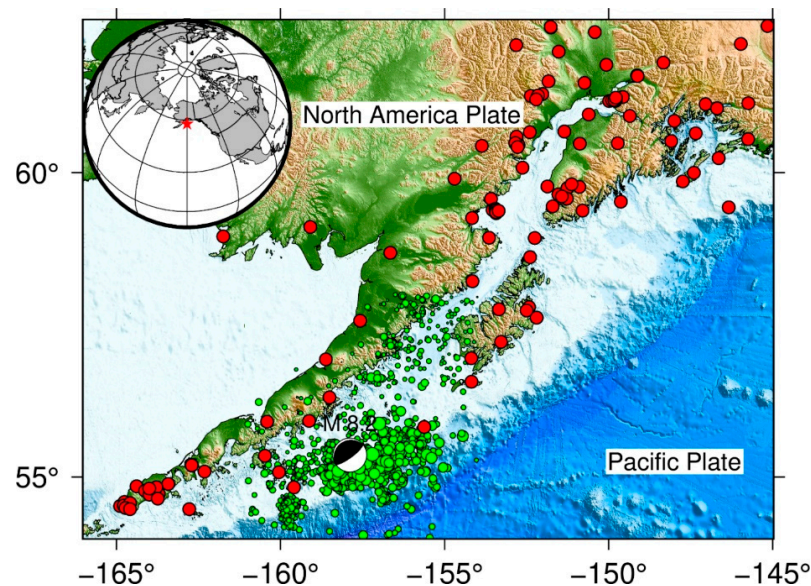


**Figure 1.** Spatial distribution of GNSS sites and the hypocenter. Red circles denote GNSS sites, and the beach ball denotes the focal mechanism of this earthquake. Green circles denote aftershocks after this earthquake, and the size of green circles denotes the magnitude of each aftershock.

As a reference, the daily GNSS solutions of near-field sites are also adopted to reveal the postseismic deformations with the time scale of days to months. The preseismic daily GNSS position time series is also included in order to estimate the linear signal caused by tectonic motion for postseismic signal modeling. The daily GNSS position time series is derived from the Nevada Geodetic Laboratory, University of Nevada, Reno (NGL/UNR). The GIPSY-OASIS-II (Version 6.1.1) software developed by Jet Propulsion Laboratory (JPL) is adopted to carry out the GNSS data processing. More details about the data processing strategy of daily GNSS position time series can be found in Blewitt et al. [36].

### 2.2. Multiscale Postseismic Signal Modeling

To insight into the very early postseismic process, the subdaily GNSS solutions are utilized to model the very early postseismic signal. Meanwhile, we also adopt the daily GNSS solutions to model the long-term postseismic signal, which can be utilized to explore long-term postseismic slip. The daily GNSS position time series is usually composed of different geophysical signals (e.g., trend signal, seasonal oscillation signal, postseismic signal, and noise). For the daily GNSS position time series, we adopt the similar data processing strategy described by Jiang et al. [37], Jiang et al. [38] and Xiang et al. [39], which can take into account the effect of the trend signal induced by tectonic motion. This data

processing strategy mainly contains outlier removal, relax time constant determination, and parameter estimation. The long-term postseismic signal captured by daily GNSS position time series can be expressed as an exponential or logarithmic model.

$$D(t) = a \times \exp(-t/b) + c \quad (1)$$

$$D(t) = a \times \ln(1 + t/b) + c \quad (2)$$

where  $a$ ,  $b$ , and  $c$  are the parameters of exponential and logarithmic model,  $t$  is the time, and  $D(t)$  is the crustal deformations. Thus, we adopt the logarithmic model to conduct the parameter estimation for the daily GNSS position time series.

In general, the exponential or logarithmic model can well describe the postseismic signal captured by daily GNSS position time series. On the other hand, the very early postseismic deformation within the first few hours following a large earthquake has a larger decay amplitude. Thus, the exponential or logarithmic model may not be suitable for modeling the transient postseismic signal detected by subdaily kinematic GNSS solutions. Liu et al. [21] suggested that the logarithmic model could not accurately delineate the very early postseismic signal, and found that the power model had better fitting performance for multiscale postseismic deformations. Thus, the power model is adopted to model the subdaily postseismic deformation, which can be expressed as:

$$D(t) = a \times t^b + c \quad (3)$$

where  $a$ ,  $b$ , and  $c$  are the parameters of the power model,  $t$  is the time, and  $D(t)$  is the crustal deformations. The kinematic GNSS position time series and the early postseismic signals modeled by the power model of near-field sites are exhibited in Figure 2.

### 2.3. Fault Slip Inversion

Based on previous studies, Wang et al. [40] developed the Steepest Descent Method (SDM) code, which can be utilized to determine fault slip under layered earth model. In this paper, the SDM code is adopted to carry out fault slip inversion, which can be expressed as:

$$f(s) = \|y - Ms\|^2 + \beta^2 \|Hs\| \quad (4)$$

$$\|Hs\| = \left\| \frac{\partial^2}{\partial x^2} \tau(s) + \frac{\partial^2}{\partial y^2} \tau(s) \right\|^2 \quad (5)$$

where  $s$  is the fault slip,  $y$  is the crustal deformation,  $M$  is the Green's function,  $H$  is the finite difference approximation of Laplacian operator,  $\tau(s)$  is the stress drop.  $\|y - Ms\|^2$  and  $\beta^2 \|Hs\|$  denote the data misfit and model roughness, and their trade-off value is usually treated as the smoothing factor (i.e.,  $\beta$ ).

On the basis of the information derived from USGS, we establish the fault model along strike and dip direction of 307.5 and 210 km, respectively. Meanwhile, we divide this fault model into 651 sub-faults with the size of  $10 \times 10$  km and compute the Green's function of dislocation using the EDGRN code [41]. The Earth model parameters used to generate the Green's function are also provided by the USGS (Table 1). According to multiscale postseismic deformations, fault model, and Green's function, the SDM code is utilized to determine the spatial distribution of very early and long-term afterslip. For the M 8.2 Chignik earthquake, some studies have characterized the coseismic slip of this earthquake using geodetic or seismological observations. Elliott et al. [28] had resolved the coseismic slip distribution of this earthquake by the combined use of static GNSS offsets, InSAR offsets, high-rate GNSS, and teleseismic waveforms. In this paper, we also present the coseismic slip of this earthquake provided by Elliott et al. [28], which can be treated as a reference of investigating the afterslip properties.

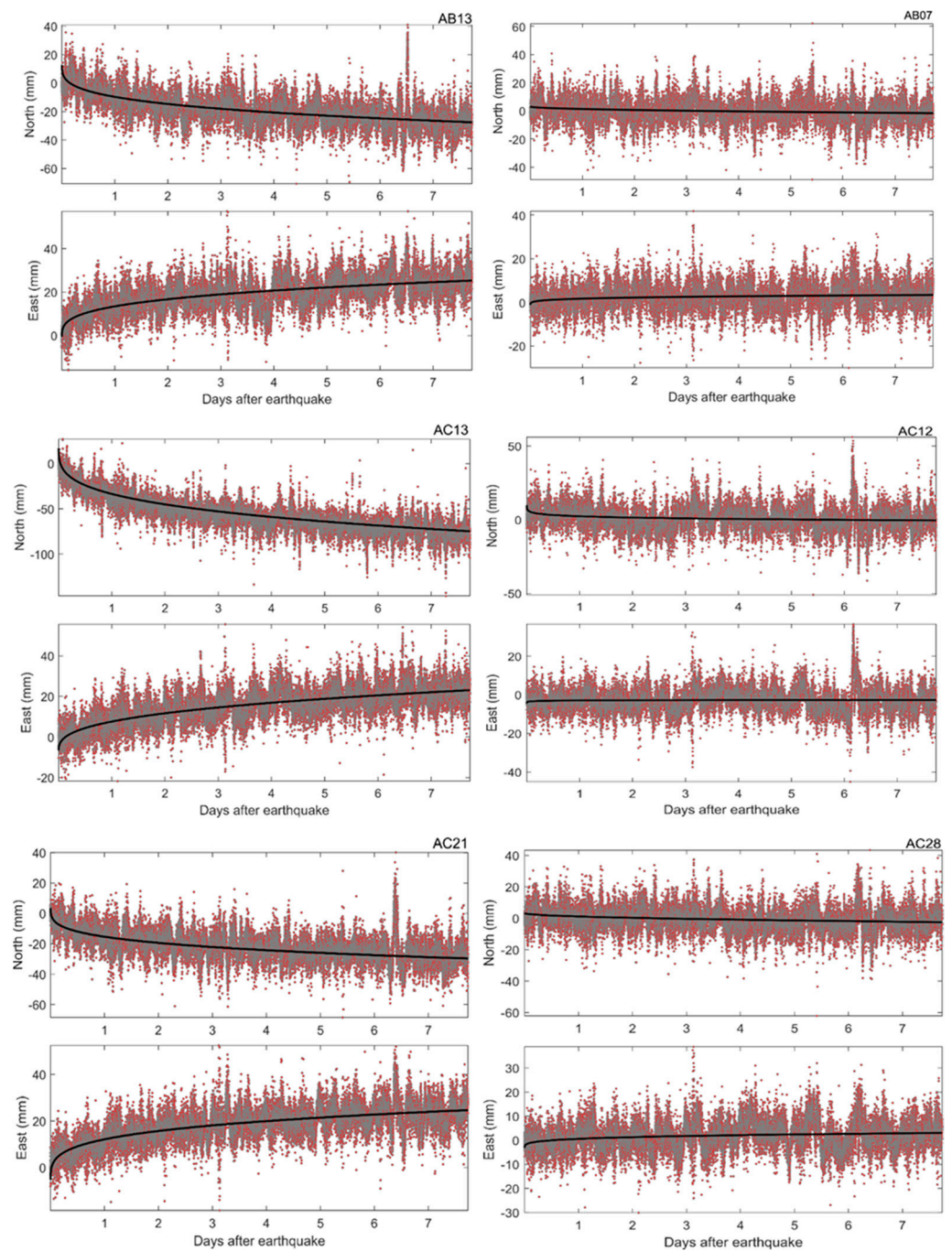


**Figure 2.** Kinematic GNSS position time series and the postseismic signals modeled by power model of 6 near-field sites.

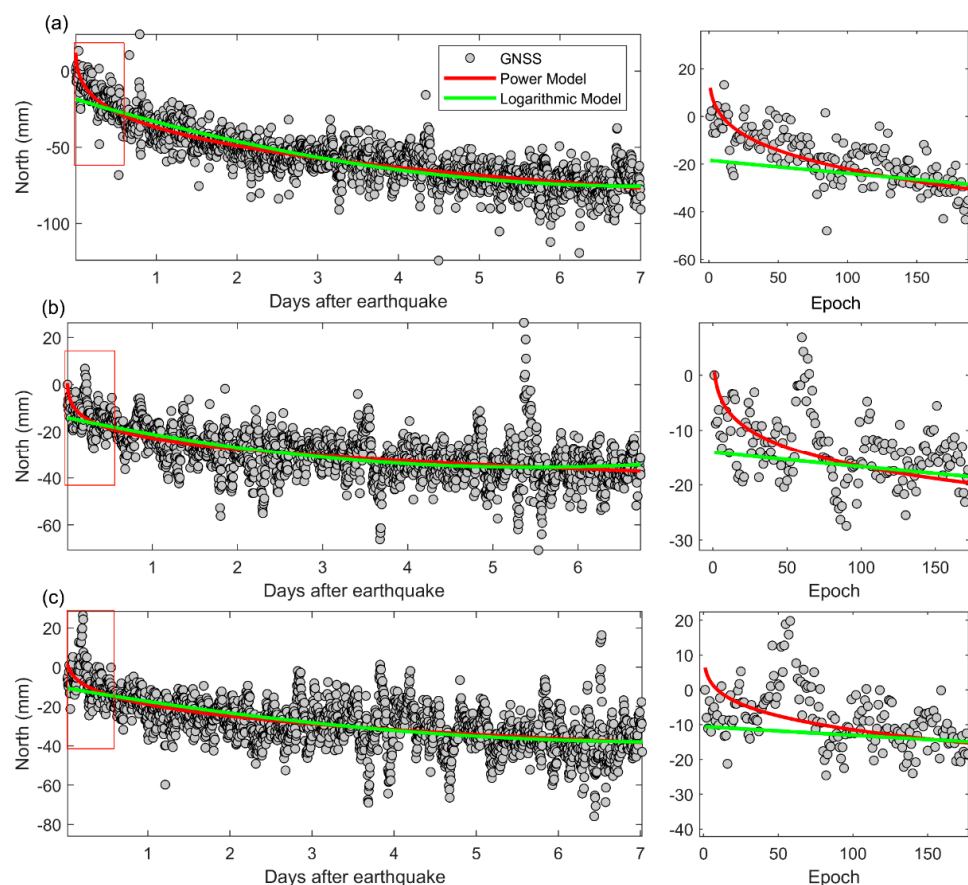
**Table 1.** The depth-variable material properties of layered halfspace used in this paper.

Depth (km)	P_Vel (km/s)	S_Vel (km/s)	Dens. (g/cm <sup>3</sup> )	Qp	Qs
0.000	2.48	0.82	1.93	1200.0	600.0
0.632	4.27	2.26	2.28	1200.0	600.0
9.917	6.35	3.68	2.75	1200.0	600.0
19.202	6.96	3.99	2.89	1200.0	600.0
27.944	7.78	4.43	3.06	1200.0	600.0
223.944	8.08	4.47	3.38	1200.0	500.0
259.944	8.60	4.66	3.45	360.0	140.0

### 3. Results

#### 3.1. Very Early Postseismic Deformations

For the M 8.2 Chignik earthquake, the 15 s kinematic GNSS solutions are adopted to detect the transient postseismic deformations within the first minutes to hours after this earthquake. Also, the daily GNSS solutions are utilized to capture the long-term postseismic deformations that can be well-fitted by the logarithmic model. On the other hand, the very early postseismic deformations captured by the subdaily GNSS solutions exhibit a larger decay rate, which may not be accurately described by the logarithmic model. To better model the postseismic signal, the kinematic GNSS position time series is slightly downsampled, which has a higher signal-to-noise ratio. As depicted in Figure 3, the logarithmic model greatly underestimates the postseismic deformations within the first hours following this earthquake, and the biases can reach several centimeters. Thus, the power function is adopted to model very early postseismic signals, and the power model can accurately depict the decay properties of very early postseismic deformations. Compared with the universal logarithmic model, the power model has better fitting performance for the very early postseismic deformations within a subdaily time scale (Table 2). Meanwhile, the later postseismic deformations after the first day can also be well modeled by the power model, which is consistent with the conclusion of Liu et al. [21].

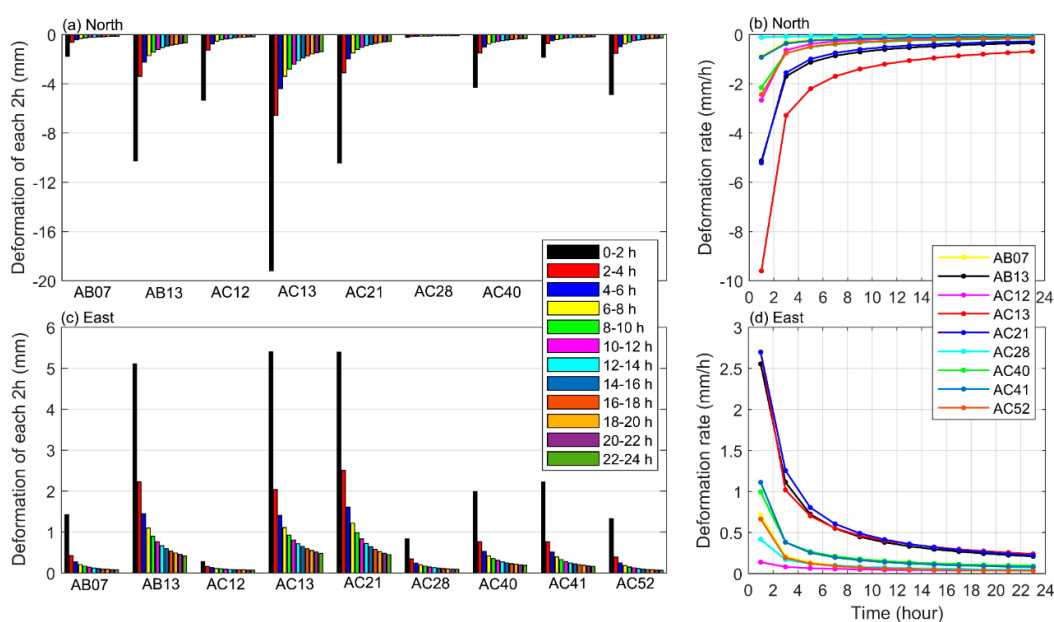


**Figure 3.** Comparison of fitting performance of power and logarithmic model. Comparison of subdaily GNSS solutions, power model, and logarithmic model for the sites AC13 (a), AC21 (b), and AB13 (c) in the north component. Red lines denote the power model, and green lines denote the logarithmic model. Right panels display the enlarged details of the left panels.

**Table 2.** Root Mean Square (RMS) error of residual time series modeled by 2 models in the north and east components.

Site	RMS (Power Model)		RMS (Logarithmic Model)	
	N (mm)	E (mm)	N (mm)	E (mm)
AB07	7.31	6.16	7.45	6.27
AB13	8.79	8.61	8.97	8.72
AC12	8.16	7.73	9.22	7.98
AC13	9.17	5.94	9.68	6.34
AC21	8.21	7.63	8.79	8.24
AC28	8.43	7.51	8.46	7.62
AC40	9.68	9.05	9.79	9.11
AC41	9.09	8.69	9.15	8.74
AC52	8.45	6.72	8.65	6.84

Considering the large noise ratio of the vertical component of kinematic GNSS solutions, Tsang et al. [18], Twardzik et al. [42], and Twardzik et al. [43] relied only on the horizontal components of kinematic GNSS solutions to characterize the distribution of very early afterslip and discarded the vertical component. In this paper, we also follow this kind of treatment strategy, and the power model is utilized to model the horizontal components of the subdaily observations of the 9 GNSS sites (Table 3). According to the modeled postseismic signal, in the 9 GNSS sites, the postseismic deformations occur, moving toward the southeast direction. The largest postseismic deformations can be observed at the site AC13, which reach  $-48.9$  and  $15.2$  mm in the north and east components during the first 24 h. Subsequently, we calculate the postseismic deformations of each 2 h and the corresponding deformation rates for the 9 GNSS sites (Figure 4). Most GNSS sites have suffered significant postseismic deformations within the first several hours following this earthquake, especially for the first 2 h. The 2 h postseismic deformations of the north and east components make up about 40% and 35% of the 24 h postseismic deformation, respectively. The 2 h postseismic deformations of site AC13 in the north and east components are  $-19.2$  and  $5.4$  mm, which make up 39.2% and 35.6% of the 24 h postseismic deformation. Meanwhile, the maximum deformation rate can reach  $9.6$  mm/h, revealing the strong fault activities during the initial phase after this earthquake.

**Figure 4.** Postseismic deformations of each 2 h (a,c) and the corresponding deformation rate (b,d) at the 9 GNSS sites in the north and east component.

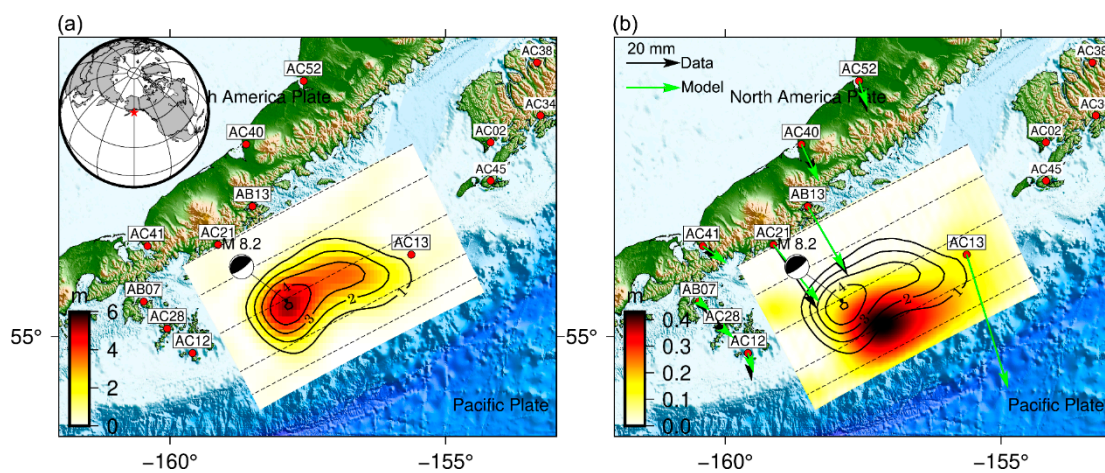
**Table 3.** The estimated power model parameters of the horizontal components of very early post seismic deformations for the 9 sites.

Site	North			East		
	a	b	c	a	b	c
AB07	−1.369	0.2606	3.164	2.049	0.1664	−0.4942
AB13	−9.81	0.2252	16.21	8.284	0.195	−15.04
AC12	−34.19	0.04556	48.45	0.05303	0.5781	−10.6
AC13	−16.31	0.2448	28.34	3.351	0.3021	−12.9
AC21	−14.99	0.1661	15.62	11.79	0.1692	−23.56
AC28	−0.02518	0.7252	0.5623	0.4042	0.3523	0.1238
AC40	−3.401	0.257	−3.286	1.17	0.3128	9.127
AC41	−1.021	0.3251	0.1114	1.868	0.2468	−10.49
AC52	−5.856	0.1904	5.045	2.121	0.1532	0

### 3.2. Spatio-Temporal Distribution of Very Early Afterslip

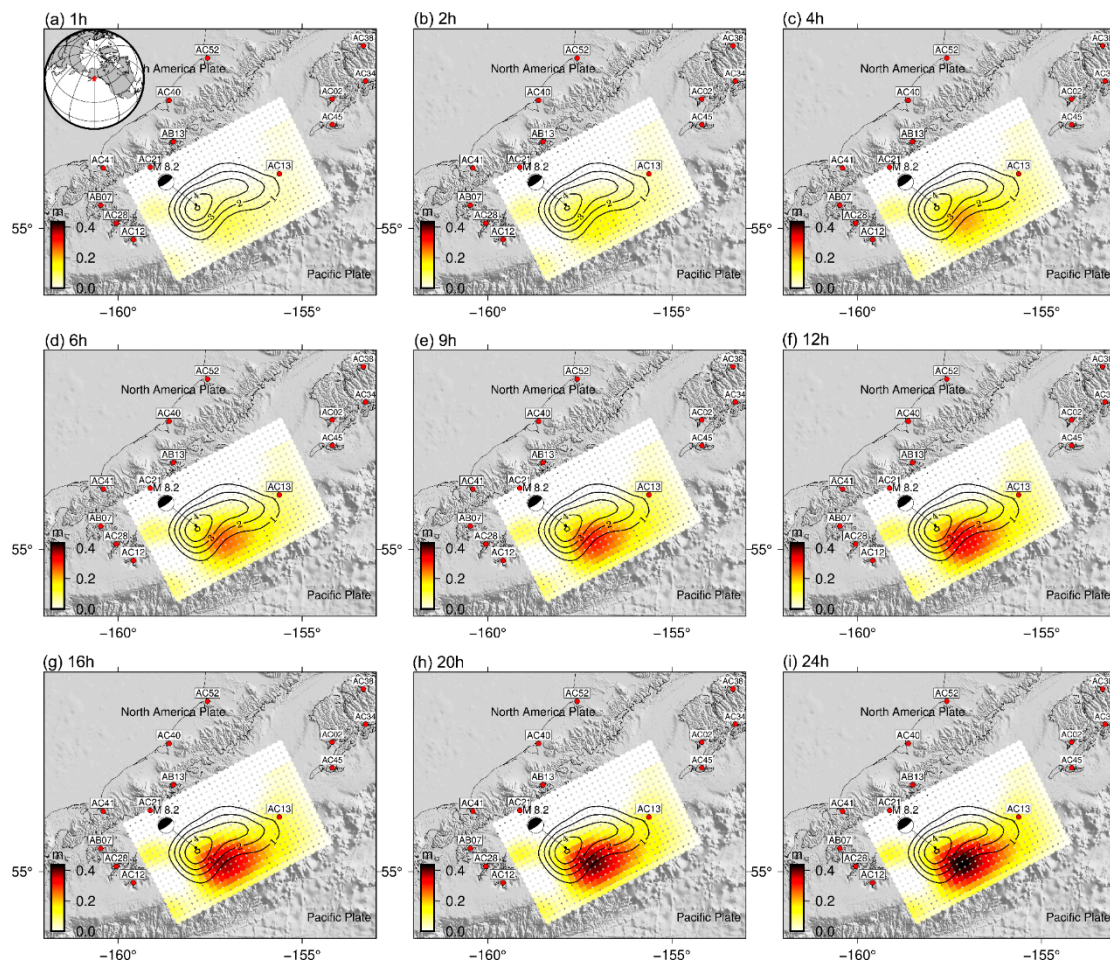
As discussed in Liu et al. [21], the influences of viscoelastic relaxation focus on the upper mantle and lower crust in the long-term period, which can be neglected in the very early postseismic phase. Thus, the very early postseismic deformations associated with this earthquake can be solely attributed to the afterslip. Following the procedure described in Section 2.3, the cumulative afterslip of the first 24 h following this earthquake is determined based on the constructed fault model and postseismic deformations. To gain the optimal fault slip, the trade-off value (i.e., 0.1) of data misfit and model roughness is treated as smoothing factor.

Figure 5a displays the coseismic slip distribution provided by Elliott et al. [28], and the maximum slip of about 6 m is situated at the depth of 32 km. Compared with coseismic slip, the cumulative afterslip of the first 24 h is mainly focused on the southeast margin of the hypocenter, implying that a shallow slip of the fault is appeared after this earthquake. Meanwhile, there is a partial overlap between coseismic slip and afterslip (Figure 5b). The maximum value of the first 24 h afterslip (i.e., 0.43 m) accounts for ~7% of the maximum coseismic slip, which is situated at the latitude of  $55.09^\circ$ , longitude of  $-157.19^\circ$ , and depth of 21.8 km. The released moment magnitude of afterslip is equal to an earthquake of ~Mw 7.4. The correlation of GNSS-derived and SDM-modeled postseismic deformations reaches 0.99, implying the result of fault slip inversion is reliable.

**Figure 5.** Coseismic slip distribution derived from Elliott et al. [28] (a) and cumulative afterslip (b) of the first 24 h following this earthquake.

Subsequently, we determine the afterslip distribution of 9 selected epochs and then generate the snapshots of the spatio-temporal evolution of afterslip during the first 24 h after this earthquake. As presented in Figure 6, the patch of afterslip is immediately

generated on the southeastern margin of the coseismic slip. The spatial distribution of this patch has not moved, but the magnitude has grown over time. The magnitude of afterslip patch varies remarkably within the 24 h following this earthquake, especially in the first several hours. The maximum afterslip of the first 4 h is 0.22 m, which makes up almost 50% of the afterslip in the 24 h. The maximum slip rate of the 24 h is about 0.018 m/h, while it reaches 0.055 m/h for the first 4 h. The results suggest that the fault activities are strong during the 24 h after the earthquake, especially in the first several hours.



**Figure 6.** Snapshots of the spatio-temporal evolution of afterslip during the first 24 h after this earthquake.

Meanwhile, we exhibit the spatio-temporal distributions of aftershocks in the near-field area (i.e., the longitude and latitude ranges are  $-160^{\circ}$  to  $-154^{\circ}$  and  $54^{\circ}$  to  $57^{\circ}$ ) within the first 24 h following this earthquake (Figure 7). The aftershock catalog is provided by USGS, and the number of aftershocks within the first 24 h reaches 293. For the first 2 h, the number of aftershocks is the highest (reaches 64), indicating the seismic activities in this time span are strong (Figure 8). Most of the aftershocks occur in the patch of afterslip, which is also located at the southeast of the hypocenter. For the other 7 time spans, almost all aftershocks appear in the area of peak after slip, especially for the last 4 time spans (i.e., 9–12 h, 12–16 h, 16–20 h, and 20–24 h). Thus, the spatio-temporal distributions of aftershocks and afterslip exhibit strong similarity during the first 24 h. Some studies have revealed the similar distributions of aftershocks and afterslip on the time scales of days to months [44]. The result confirms that the similar distributions of aftershocks and afterslip also exist within the first several hours after this earthquake. Moreover, the result suggests that the very early afterslip may be a triggering mechanism for aftershocks in addition to the effects of coseismic stress.

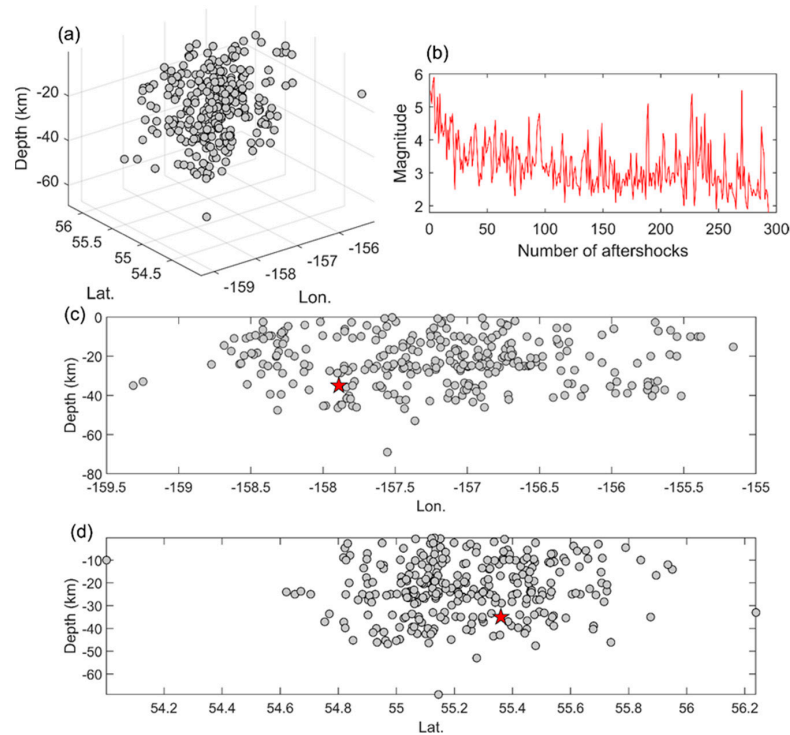


**Figure 7.** Daily spatial distribution of aftershocks and afterslip during the time span of 0–7 days for the first 7 days. (a) is the 3D pattern of aftershocks. (b) is the magnitude of aftershocks. (c,d) are the distributions of aftershocks along longitude and latitude, respectively.

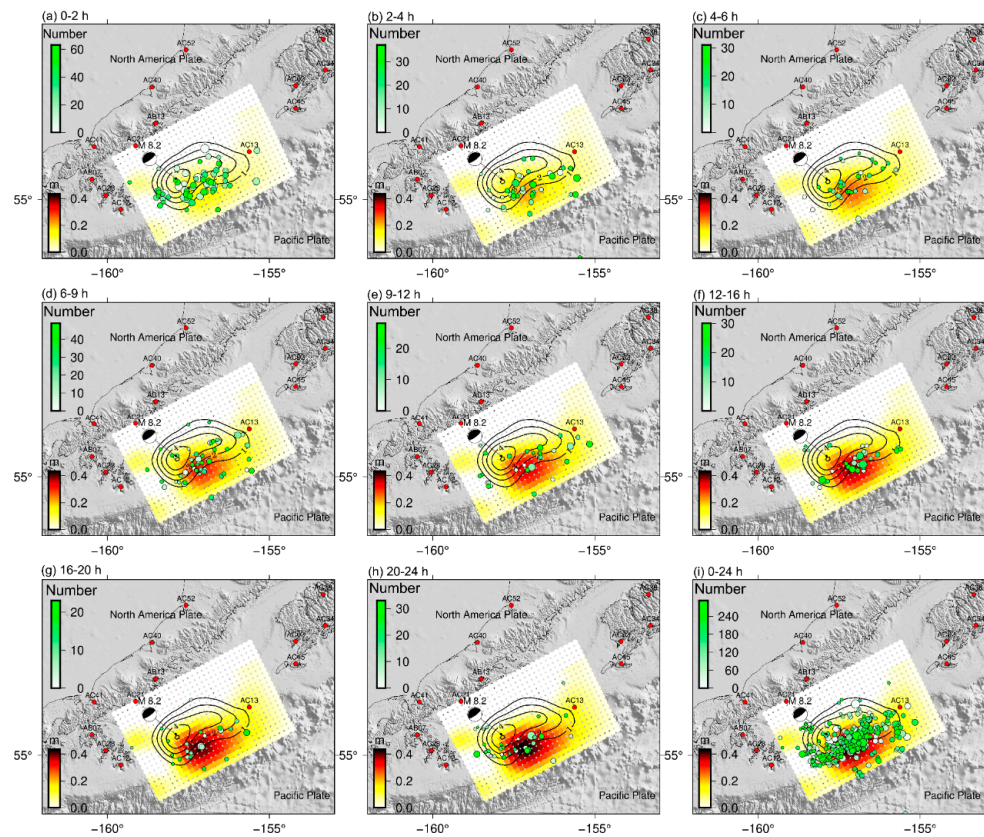


**Figure 8.** Spatio-temporal distributions of afterslip and aftershocks during the first 24 h after this earthquake. The green scale denotes the number of aftershocks counted by the occurrence time of aftershocks.

### 3.3. Comparison of Afterslip Estimated by Daily and Subdaily Solutions

In order to assess the bias of the afterslip estimated by daily solution, we make a comparison of the afterslip determined by daily and subdaily GNSS solution, and then highlight the important contributions of the very early afterslip. Firstly, we compare the 48 h afterslip estimated by kinematic GNSS solutions with the 2 days afterslip determined by daily solutions. As illustrated in Figure 9a, the 48 h and 2 days afterslip models exhibit similar spatial distribution, but the magnitude of the 48 h afterslip model is significantly larger. The maximum value of 48 h afterslip is 0.53 m, and the released moment magnitude is equivalent to  $\sim$ Mw 7.4. On the other hand, the maximum value of 2 days afterslip is 0.21 m with a seismic moment magnitude of  $\sim$ Mw 7.1. The positive biases are mainly focused on the afterslip patch. The result implies that neglecting very early afterslip can lead to the underestimation of postseismic slip, which in turn can bias our perception of coseismic and postseismic processes.

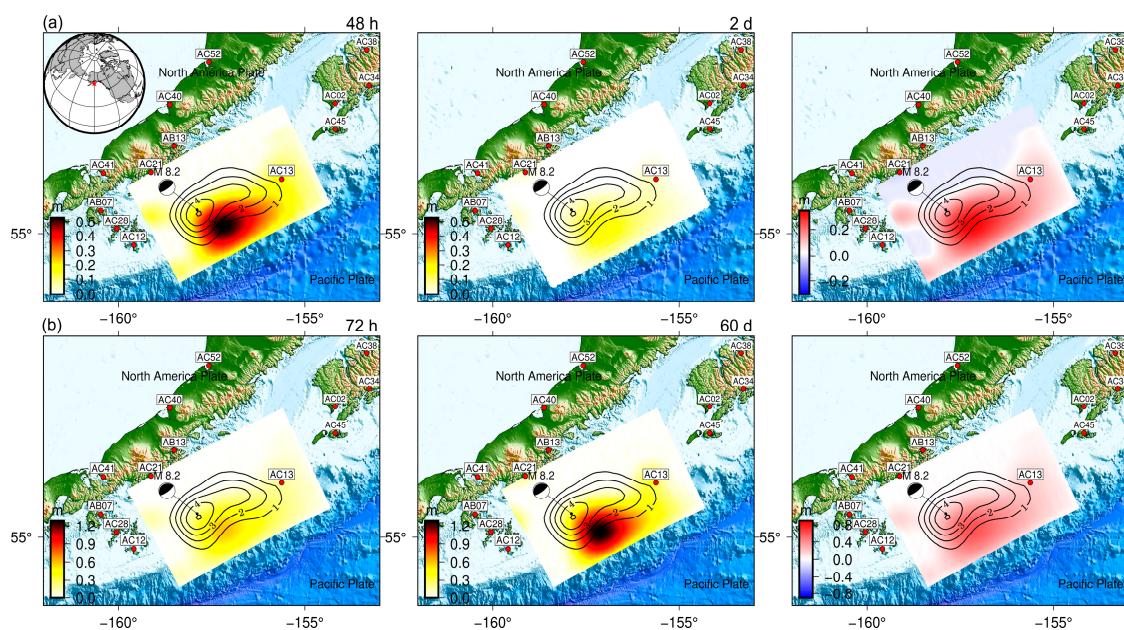


**Figure 9.** Comparison of afterslip estimated by daily and subdaily solutions. (a) Spatial patterns of the afterslip determined by 48 h subdaily and 2 days daily GNSS solutions. (b) Spatial patterns of the afterslip determined by 72 h subdaily and 60 days daily GNSS solutions.

Moreover, we also display the 60-day afterslip determined by daily GNSS solutions, which is compared with the 72 h afterslip estimated by subdaily solutions (Figure 9b). As described in Section 3.2, the patch of afterslip is immediately generated after the earthquake, and the postseismic slip continues along the afterslip patch. For the 60-day afterslip, this patch seems to nucleate at the southeast edge of the hypocenter, and the maximum value of the afterslip reaches 1.29 m. As for the 72 h afterslip, the maximum value of the afterslip is 0.60 m, which accounts for  $\sim$ 60% of the maximum value of 60 days afterslip. The result further highlights that fault activities are particularly intense in the early postseismic period, and the coseismic stress is rapidly unloaded as part of the fault relaxation process. Thus, insight into very early postseismic deformations can help to accurately characterize the amount of afterslip and better understand the transition process from coseismic rupture to postseismic relaxation.

## 4. Discussion

### 4.1. Coseismic Coulomb Stress Variations

In general, the stress state around the coseismic rupture area can be changed after the earthquake. The Coulomb Stress Change (CSC) generated by coseismic rupture is

usually considered to be related to postseismic activities. Thus, the coseismic coulomb stress changes associated with this earthquake are investigated to evaluate the seismic hazards and understand the driving mechanism of postseismic activities (e.g., afterslip and aftershocks). In this paper, the Coulomb 3.4 software is adopted to estimate the coseismic CSC of this earthquake based on the Coulomb failure criterion [45–48]. The effective friction coefficient is set as 0.4, which has been widely utilized in many previous studies. The optimal nodal plane of the moment tensor solution derived from USGS (strike =  $239^\circ$ , dip =  $14^\circ$ , and rake =  $95^\circ$ ) is regarded as the parameters of receiver fault for CSC estimation.

As depicted in Figure 10, the CSC generated by the coseismic rupture of this earthquake is estimated. The CSC along the rupture fault indicates that the coseismic rupture area is dominated by the negative CSC, implying that the cumulative stress before this earthquake is significantly released. On the other hand, the area surrounding coseismic rupture is occupied by positive CSC. Thus, most of the afterslip patch is situated at the positive CSC area according to the spatial patterns of afterslip and Coulomb stress, which suggests that the coseismic CSC in the surrounding area may be the driving factor of afterslip. Subsequently, we exhibit the coseismic CSC at depths of maximum coseismic and postseismic slip (i.e., 22 and 34 km), and the aftershocks within the first 3 days after this earthquake are also displayed. Compared with the aftershocks within the first 24 h, the number and magnitude of the aftershocks within the next 2 days are significantly smaller. For the CSC at the two depths, most of the aftershocks within the first 24 days are situated at the high-to-low CSC area, while the aftershocks within the next 2 days are focused on the positive CSC area. Section 3.2 revealed that the spatio-temporal distributions of aftershocks and afterslips exhibit strong similarity. Thus, the immediate afterslip and aftershocks may be influenced by the coseismic CSC generated by this earthquake, and the evolving afterslip may also affect the spatio-temporal variations of aftershocks.

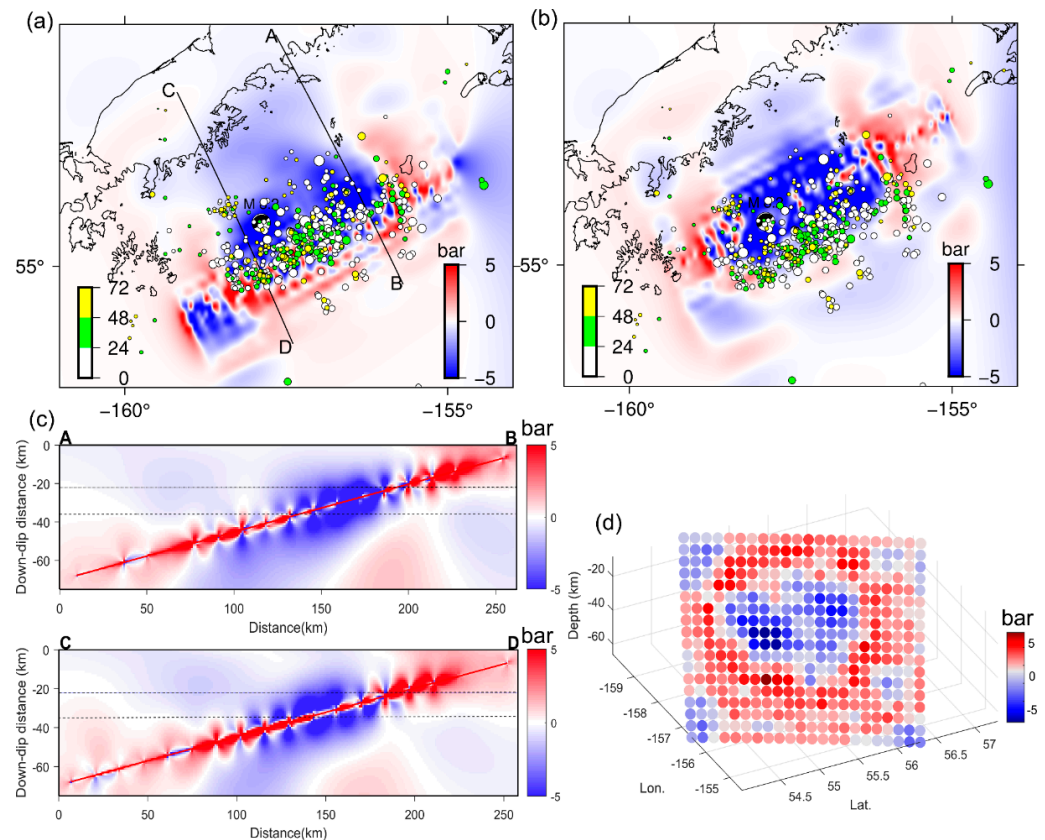


**Figure 10.** Coulomb Stress Changes (CSC) generated by coseismic rupture of this earthquake. (a) Coseismic CSC at a depth of 22 km. (b) Coseismic CSC at a depth of 34 km. (c) Two cross-sections of CSC along the lines displayed in (a). (d) Coseismic CSC along the receiver fault.

#### 4.2. Possible Triggering Mechanisms for Very Early Aftershocks

Aftershock is an important postseismic activity, but the triggering mechanism of the aftershock remains controversial [49–51]. Aftershocks are generally considered to be associated with the Coulomb stress generated by coseismic rupture. In addition to the impacts of coseismic rupture, some studies have tried to evaluate the role of afterslip in the triggering of aftershocks. Afterslip is treated as a possible triggering mechanism of aftershocks due to the high similarity between the spatial patterns of aftershocks and afterslip. On the other hand, most relevant studies mainly focus on the time scale of days to months after the earthquake [52]. Recently, some studies have paid gradual attention to the afterslip–aftershock relationship during the very early postseismic phase using subdaily geodetic observations.

In this paper, based on the subdaily GNSS solutions, the afterslip–aftershock relationship in the very early postseismic period (i.e., first 24 h) after the M 8.2 Chignik earthquake is investigated (Figure 8). Overall, most of the aftershocks during the first 24 h are distributed in the area that suffered from afterslip (i.e., the shallow updip area). Meanwhile, the spatial patterns of afterslips and aftershocks are highly consistent and also exhibit similar spatio-temporal evolution features. For the first 2 h, some aftershocks occurring immediately after the earthquake are distributed around the hypocenter. The other aftershocks occur within the afterslip patch, which is situated at the southeast of the hypocenter. Over the next two time periods (i.e., 2–4 h and 4–6 h), the aftershock activities seem to be migrating towards the peak afterslip area. During the last four time periods, almost all aftershocks occurred in the peak afterslip area. Thus, the aftershocks may be influenced by the fault behaviors (i.e., afterslip) during the first 24 h after this earthquake, which can be explained by the unstable failure of small asperities loaded by the afterslip process.

Meanwhile, the stress changes induced by coseismic rupture also play an important role in the triggering of afterslip and aftershock activities. As discussed in Section 4.1, the coseismic rupture area is dominated by negative CSC, whereas positive CSC can be observed in the surrounding area. The shallow afterslip is situated at the southeast margin of the hypocenter, where the positive CSC is distributed. To a certain extent, the afterslip occurring immediately after the earthquake may be driven by coseismic CSC, implying that the immediate afterslip and aftershock activities can be influenced by the coseismic CSC. The following afterslip process further releases coseismic CSC and then influences the spatio-temporal variations of aftershock activities. Therefore, very early aftershocks may be triggered by afterslip together with coseismic CSC. On the other hand, the postseismic process is usually affected by a variety of geophysical factors, so the triggering of aftershocks cannot be solely attributed to the afterslip and CSC. Of course, other geophysical factors (e.g., fluid flow and viscoelastic relaxation) included in the postseismic process may also be responsible for aftershock generation, and this needs to be explored further.

In addition, Twardzik et al. [43] also assessed the relationship between very early afterslips and aftershocks following the 2015 Mw 8.3 Illapel, Chile earthquake and discussed the potential to predict aftershock location using very early post-seismic observations. Currently, most physics-based aftershock sequence models used for prediction do not contain information about postseismic slip. For some earthquakes, apart from the factors of coseismic rupture, the early afterslip may be an important triggering mechanism of aftershocks. Thus, rapid imaging of very early afterslips can provide important information to forecast the spatial distribution of aftershocks. On the other hand, the challenge lies in obtaining postseismic deformations with little time latency. Meanwhile, whether the information provided by the very early afterslip has the potential to predict the spatial pattern of aftershocks needs to be further explored and confirmed.

## 5. Conclusions

The very early postseismic deformations associated with the Chignik earthquake are detected by the kinematic solutions of near-field GNSS sites. Compared with the logarithmic or exponential model, the subdaily GNSS position time series can be well-

fitted by the power model. The spatial pattern of very early afterslip is characterized based on GNSS-modeled postseismic signals and the constructed fault model. A shallow updip afterslip can be observed after this earthquake, which is situated southeast of the hypocenter. Compared with the afterslip estimated by daily GNSS solutions, it can be found that the postseismic slip will be greatly underestimated if the very early afterslip is not fully considered. The spatio-temporal distributions of very early afterslips and aftershocks during the first 24 h after this earthquake are also revealed, and the spatio-temporal patterns of afterslips and aftershocks are highly consistent. Meanwhile, most of the afterslip patches and aftershocks occurring immediately after this earthquake are situated in the positive CSC area. Thus, in addition to the Coulomb stress changes induced by coseismic rupture, the very early afterslip may be a possible driving factor of aftershocks during the early postseismic phase.

**Author Contributions:** Conceptualization, Y.X. (Yunfei Xiang) and Y.B.; methodology, Y.B. and J.L.; formal analysis, Y.B. and Y.X. (Yin Xing); data curation, J.L. and Y.X. (Yin Xing); writing—original draft preparation, Y.X. (Yunfei Xiang); writing—review and editing, Y.X. (Yunfei Xiang); supervision, Y.B.; funding acquisition, Y.X. (Yunfei Xiang). All authors have read and agreed to the published version of the manuscript.

**Funding:** This study is funded by National Natural Science Foundation of China (Grant number 42304016, Funder: Yunfei Xiang) and Basic Science (Natural Science) Research Project for Colleges and Universities of Jiangsu Province (Grant number 22KJB420002, Funder: Yunfei Xiang).

**Data Availability Statement:** The daily GNSS position time series derived from NGL/NUR is available at [http://geodesy.unr.edu/gps\\_timeseries/tenv/](http://geodesy.unr.edu/gps_timeseries/tenv/) (accessed on 25 June 2023). The 15 s GNSS observations is available at <https://data.unavco.org/archive/gnss/rinex/obs/2021/> (accessed on 25 June 2023). The relevant information associated with the 2021 M 8.2 Chignik, Alaska earthquake can be acquired from <https://earthquake.usgs.gov/earthquakes/eventpage/ak0219neiszm/> (accessed on 15 July 2023). Aftershock catalog provided by USGS is obtained from <https://earthquake.usgs.gov/earthquakes/search/> (accessed on 15 July 2023).

**Acknowledgments:** We are very grateful to Nevada Geodetic Laboratory, University of Nevada, Reno (NGL/UNR) and University NAVSTAR Consortium (UNAVCO) for providing daily GNSS position time series and 15 s GNSS observations, respectively. We are also very grateful to United States Geological Survey (USGS) for providing the early aftershock catalog following the 2021 M 8.2 Chignik, Alaska earthquake.

**Conflicts of Interest:** The authors declare no conflict of interest.

## References

1. Hsu, Y.J.; Simons, M.; Avouac, J.P.; Galetzka, J.; Sieh, K.; Chlieh, M.; Natawidjaja, D.; Prawirodirdjo, L.; Bock, Y. Frictional afterslip following the 2005 Nias-Simeulue earthquake, Sumatra. *Science* **2006**, *312*, 1921–1926. [[CrossRef](#)]
2. Barbot, S.; Fialko, Y.; Bock, Y. Postseismic deformation due to the Mw 6.0 2004 Parkfield earthquake: Stress-driven creep on a fault with spatially variable rate-and-state friction parameters. *J. Geophys. Res. Solid Earth* **2009**, *114*, B07405. [[CrossRef](#)]
3. Huang, M.H.; Bürgmann, R.; Freed, A.M. Probing the lithospheric rheology across the eastern margin of the Tibetan Plateau. *Earth Planet. Sci. Lett.* **2014**, *396*, 88–96. [[CrossRef](#)]
4. McCormack, K.; Hesse, M.A.; Dixon, T.H.; Malservisi, R. Modeling the contribution of poroelastic deformation to postseismic geodetic signals. *Geophys. Res. Lett.* **2020**, *47*, e2020GL086945. [[CrossRef](#)]
5. Freed, A.M. Afterslip (and only afterslip) following the 2004 Parkfield California earthquake. *Geophys. Res. Lett.* **2007**, *34*, L06312. [[CrossRef](#)]
6. Avouac, J.P. From geodetic imaging of seismic and aseismic fault slip to dynamic modeling of the seismic cycle. *Annu. Rev. Earth Planet. Sci.* **2015**, *43*, 233–271. [[CrossRef](#)]
7. Bürgmann, R. The geophysics, geology and mechanics of slow fault slip. *Earth Planet. Sci. Lett.* **2018**, *495*, 112–134. [[CrossRef](#)]
8. Tian, Z.; Freymueller, J.T.; Yang, Z. Postseismic deformation due to the 2012 Mw 7.8 Haida Gwaii and 2013 Mw 7.5 Craig earthquakes and its implications for regional rheological structure. *J. Geophys. Res. Solid Earth* **2021**, *126*, e2020JB020197. [[CrossRef](#)]
9. Churchill, R.M.; Werner, M.J.; Biggs, J.; Fagereng, Å. Afterslip moment scaling and variability from a global compilation of estimates. *J. Geophys. Res. Solid Earth* **2022**, *127*, e2021JB023897. [[CrossRef](#)]
10. Elliott, J.R.; Walters, R.J.; Wright, T.J. The Role of Space-Based Observation in Understanding and Responding to Active Tectonics and Earthquakes. *Nat. Commun.* **2016**, *7*, 13844. [[CrossRef](#)]

11. Malservisi, R.; Schwartz, S.Y.; Voss, N.; Protti, M.; Gonzalez, V.; Dixon, T.H.; Jiang, Y.; Newman, A.V.; Richardson, J.; Walter, J.I.; et al. Multiscale postseismic behavior on a megathrust: The 2012 Nicoya earthquake, Costa Rica. *Geochem. Geophys. Geosystems* **2015**, *16*, 1848–1864. [[CrossRef](#)]
12. Golriz, D.; Bock, Y.; Xu, X. Defining the coseismic phase of the crustal deformation cycle with seismogeodesy. *J. Geophys. Res. Solid Earth* **2021**, *126*, e2021JB022002. [[CrossRef](#)]
13. Peng, Z.; Zhao, P. Migration of early aftershocks following the 2004 Parkfield earthquake. *Nat. Geosci.* **2009**, *2*, 877–881. [[CrossRef](#)]
14. Lange, D.; Bedford, J.R.; Moreno, M.; Tilmann, F.; Baez, J.C.; Bevis, M.; Krüger, F. Comparison of postseismic afterslip models with aftershock seismicity for three subduction-zone earthquakes: Nias 2005, Maule 2010 and Tohoku 2011. *Geophys. J. Int.* **2014**, *199*, 784–799. [[CrossRef](#)]
15. Ross, Z.E.; Rollins, C.; Cochran, E.S.; Hauksson, E.; Avouac, J.P.; Ben-Zion, Y. Aftershocks driven by afterslip and fluid pressure sweeping through a fault-fracture mesh. *Geophys. Res. Lett.* **2017**, *44*, 8260–8267. [[CrossRef](#)]
16. Perfettini, H.; Frank, W.B.; Marsan, D.; Bouchon, M. A model of aftershock migration driven by afterslip. *Geophys. Res. Lett.* **2018**, *45*, 2283–2293. [[CrossRef](#)]
17. Perfettini, H.; Frank, W.B.; Marsan, D.; Bouchon, M. Updip and along-strike aftershock migration model driven by afterslip: Application to the 2011 Tohoku-Oki aftershock sequence. *J. Geophys. Res. Solid Earth* **2019**, *124*, 2653–2669. [[CrossRef](#)]
18. Tsang, L.L.; Vergnolle, M.; Twardzik, C.; Sladen, A.; Nocquet, J.-M.; Rolandone, F.; Agurto-Detzel, H.; Cavalié, O.; Jarrin, P.; Mothes, P. Imaging rapid early afterslip of the 2016 Pedernales earthquake, Ecuador. *Earth Planet. Sci. Lett.* **2019**, *524*, 115724. [[CrossRef](#)]
19. Milliner, C.; Bürgmann, R.; Inbal, A.; Wang, T.; Liang, C. Resolving the kinematics and moment release of early afterslip within the first hours following the 2016 Mw 7.1 Kumamoto earthquake: Implications for the shallow slip deficit and frictional behavior of aseismic creep. *J. Geophys. Res. Solid Earth* **2020**, *125*, e2019JB018928. [[CrossRef](#)]
20. Jiang, J.; Bock, Y.; Klein, E. Coevolving early afterslip and aftershock signatures of a San Andreas fault rupture. *Sci. Adv.* **2021**, *7*, eabc1606. [[CrossRef](#)]
21. Liu, K.; Geng, J.; Wen, Y.; Ortega-Culaciati, F.; Comte, D. Very early postseismic deformation following the 2015 Mw 8.3 Illapel earthquake, Chile revealed from kinematic GPS. *Geophys. Res. Lett.* **2022**, *49*, e2022GL098526. [[CrossRef](#)]
22. Periollat, A.; Radiguet, M.; Weiss, J.; Twardzik, C.; Amitrano, D.; Cotte, N.; Marill, L.; Socquet, A. Transient brittle creep mechanism explains early postseismic phase of the 2011 Tohoku-Oki megathrust earthquake: Observations by high-rate GPS solutions. *J. Geophys. Res. Solid Earth* **2022**, *127*, e2022JB024005. [[CrossRef](#)]
23. Crowell, B.W.; Melgar, D. Slipping the Shumagin Gap: A kinematic coseismic and early afterslip model of the Mw 7.8 Simeonof Island, Alaska, earthquake. *Geophys. Res. Lett.* **2020**, *47*, e2020GL090308. [[CrossRef](#)]
24. Li, S.; Freymueller, J.T. Spatial variation of slip behavior beneath the Alaska Peninsula along Alaska-Aleutian subduction zone. *Geophys. Res. Lett.* **2018**, *45*, 3453–3460. [[CrossRef](#)]
25. Liu, C.; Lay, T.; Xiong, X.; Wen, Y. Rupture of the 2020 Mw 7.8 earthquake in the Shumagin gap inferred from seismic and geodetic observations. *Geophys. Res. Lett.* **2020**, *47*, e2020GL090806. [[CrossRef](#)]
26. Xiao, Z.; Freymueller, J.T.; Grapenthin, R.; Elliott, J.L.; Drooff, C.; Fusso, L. The deep shumagin gap filled: Kinematic rupture model and slip budget analysis of the 2020 Mw 7.8 simeonof earthquake constrained by GNSS, global seismic waveforms, and floating InSAR. *Earth Planet. Sci. Lett.* **2021**, *576*, 117241. [[CrossRef](#)]
27. Liu, C.; Lay, T.; Xiong, X. The 29 July 2021 MW 8.2 Chignik, Alaska Peninsula earthquake rupture inferred from seismic and geodetic observations: Re-rupture of the western 2/3 of the 1938 rupture zone. *Geophys. Res. Lett.* **2022**, *49*, e2021GL096004. [[CrossRef](#)]
28. Elliott, J.L.; Grapenthin, R.; Parameswaran, R.; Xiao, Z.; Freymueller, J.; Logan, F. Cascading rupture of a megathrust. *Sci. Adv.* **2022**, *8*, eabm4131. [[CrossRef](#)]
29. Brooks, B.A.; Goldberg, D.; DeSanto, J.; Ericksen, T.L.; Webb, S.C.; Nooner, S.L.; Chadwell, C.D.; Foster, J.; Minson, S.; Witter, R.; et al. Rapid shallow megathrust afterslip from the 2021 M 8.2 Chignik, Alaska earthquake revealed by seafloor geodesy. *Sci. Adv.* **2023**, *9*, eadf9299. [[CrossRef](#)]
30. Geng, J.; Chen, X.; Pan, Y.; Mao, S.; Li, C.; Zhou, J.; Zhang, K. PRIDE PPP-AR: An open-source software for GPS PPP ambiguity resolution. *GPS Solut.* **2019**, *23*, 91. [[CrossRef](#)]
31. Geng, J.; Chen, X.; Pan, Y.; Zhao, Q. A modified phase clock/bias model to improve PPP ambiguity resolution at Wuhan University. *J. Geod.* **2019**, *93*, 2053–2067. [[CrossRef](#)]
32. Geng, J.; Wen, Q.; Zhang, Q.; Li, G.; Zhang, K. GNSS observable-specific phase biases for all-frequency PPP ambiguity resolution. *J. Geod.* **2022**, *96*, 11. [[CrossRef](#)]
33. Zheng, J.Z.; Guo, F. An adaptive stochastic model for GPS observations and its performance in precise point positioning. *Surv. Rev.* **2016**, *48*, 296–302. [[CrossRef](#)]
34. Wei, H.H.; Yu, T.N.; Tu, J.S.; Ke, F.Y. Detection and Evaluation of Flood Inundation Using CYGNSS Data during Extreme Precipitation in 2022 in Guangdong Province, China. *Remote Sens.* **2023**, *15*, 297. [[CrossRef](#)]
35. Wei, H.H.; He, X.F.; Feng, Y.M.; Jin, S.G.; Shen, F. Snow depth estimation on slopes using GPS-Interferometric reflectometry. *Sensors* **2019**, *19*, 4994. [[CrossRef](#)] [[PubMed](#)]
36. Blewitt, G.; Hammond, W.C.; Kreemer, C. Harnessing the GPS data explosion for interdisciplinary science. *Eos* **2018**, *99*. [[CrossRef](#)]

37. Jiang, Z.S.; Yuan, L.; Huang, D.; Yang, Z.; Hassan, A. Postseismic deformation associated with the 2015 Mw 7.8 Gorkha earthquake, Nepal: Investigating ongoing afterslip and constraining crustal rheology. *J. Asian Earth Sci.* **2018**, *156*, 1–10. [[CrossRef](#)]
38. Jiang, Z.S.; Huang, D.; Yuan, L.; Hassan, A.; Zhang, L.; Yang, Z. Coseismic and postseismic deformation associated with the 2016 Mw 7.8 Kaikoura earthquake, New Zealand: Fault movement investigation and seismic hazard analysis. *Earth Planets Space* **2018**, *70*, 62. [[CrossRef](#)]
39. Xiang, Y.F.; Yue, J.P.; Jiang, Z.S.; Xing, Y. Spatial-temporal properties of afterslip associated with the 2015 Mw 8.3 Illapel earthquake, Chile. *Earth Planets Space* **2021**, *73*, 27. [[CrossRef](#)]
40. Wang, R.; Diao, F.; Hoechner, A. SDM—A geodetic inversion code 605 incorporating with layered crust structure and curved fault geometry. In Proceedings of the EGU General Assembly 2013, Vienna, Austria, 7–12 April 2013; EGU2013-2411-1.
41. Wang, R.; Martin, F.L.; Roth, F. Computation of deformation induced by earthquakes in a multi-layered elastic crust—FORTRAN programs EDGRN/EDCMP. *Comput. Geosci.* **2003**, *29*, 195–207. [[CrossRef](#)]
42. Twardzik, C.; Vergnolle, M.; Sladen, A.; Avallone, A. Unravelling the contribution of early postseismic deformation using sub-daily GNSS positioning. *Sci. Rep.* **2019**, *9*, 1175. [[CrossRef](#)]
43. Twardzik, C.; Vergnolle, M.; Sladen, A.; Tsang, L.L.H. Very early identification of a bimodal frictional behavior during the post-seismic phase of the 2015 Mw 8.3 Illapel, Chile, earthquake. *Solid Earth* **2021**, *12*, 2523–2537. [[CrossRef](#)]
44. Perfettini, H.; Avouac, J.P. Modeling afterslip and aftershocks following the 1992 Landers earthquake. *J. Geophys. Res. Solid Earth* **2007**, *112*, B07409. [[CrossRef](#)]
45. Lin, J.; Stein, R.S. Stress triggering in thrust and subduction earthquakes, and stress interaction between the southern San Andreas and nearby thrust and strike-slip faults. *J. Geophys. Res. Solid Earth* **2004**, *109*, B02303. [[CrossRef](#)]
46. Freed, A.M. Earthquake triggering by static, dynamic, and postseismic stress transfer. *Annu. Rev. Earth Planet. Sci.* **2005**, *33*, 335–367. [[CrossRef](#)]
47. Toda, S.; Stein, R.S.; Richards-Dinger, K.; Bozkurt, S. Forecasting the evolution of seismicity in southern California: Animations built on earthquake stress transfer. *J. Geophys. Res.* **2005**, *110*, B05S16. [[CrossRef](#)]
48. Toda, S.; Stein, R.S.; Sevilgen, V.; Lin, J. *Coulomb 3.3 Graphic-Rich Deformation and Stress-Change Software for Earthquake, Tectonic, and Volcano Research and Teaching—User Guide*; 2011–1060; Earthquake Science Center, Menlo Park Science Center: Menlo Park, CA, USA, 2011.
49. Mignan, A. Modeling aftershocks as a stretched exponential relaxation. *Geophys. Res. Lett.* **2015**, *42*, 9726–9732. [[CrossRef](#)]
50. Miller, S.A. Aftershocks are fluid-driven and decay rates controlled by permeability dynamics. *Nat. Commun.* **2020**, *11*, 5787. [[CrossRef](#)]
51. Ozawa, S.; Ando, R. Mainshock and Aftershock Sequence Simulation in Geometrically Complex Fault Zones. *J. Geophys. Res. Solid Earth* **2021**, *126*, e2020JB020865. [[CrossRef](#)]
52. Frank, W.B.; Poli, P.; Perfettini, H. Mapping the rheology of the Central Chile subduction zone with aftershocks. *Geophys. Res. Lett.* **2017**, *44*, 5374–5382. [[CrossRef](#)]

**Disclaimer/Publisher’s Note:** The statements, opinions and data contained in all publications are solely those of the individual author(s) and contributor(s) and not of MDPI and/or the editor(s). MDPI and/or the editor(s) disclaim responsibility for any injury to people or property resulting from any ideas, methods, instructions or products referred to in the content.